Scripta Materialia 162 (2019) 156–160

Contents lists available at ScienceDirect

Scripta Materialia

journal homepage: www.elsevier.com/locate/scriptamat

Helium irradiation of Y_2O_3-Fe bilayer system

A. Mairov [a,*], D. Frazer [b,1], P. Hosemann [b], K. Sridharan [a]

[a] Department of Engineering Physics, University of Wisconsin-Madison, Madison, WI 53706, USA
[b] Department of Nuclear Engineering, University of California-Berkeley, Berkeley, CA 94720, USA

ARTICLE INFO

Article history:
Received 21 August 2018
Received in revised form 20 October 2018
Accepted 1 November 2018
Available online xxxx

Keywords:
Thin films
Interface wetting
Helium bubbles
STEM
ODS

ABSTRACT

Y_2O_3/Fe bilayer systems and associated interfaces with different crystallographic orientations were implanted with helium. High resolution scanning transmission electron microscopy (HRSTEM) analysis showed that implanted helium formed larger sized bubbles at the interface than within the individual film layers. The bubbles at the interface were located on the oxide side of the interface and only "wetted" a small area of the interface. In contrast, bubbles nucleating at grain boundaries within the iron layer were observed to symmetrically form across the grain boundaries, suggesting remarkable differences in helium bubble nucleation between metal/oxide interfaces and grain boundaries in metals.

Helium can form in structural materials in a nuclear reactor either by neutron-induced (n,α) transmutation reactions or by the impingement of α particles on the surface of the material as, for example, first wall of fusion reactors. Helium is mostly insoluble in metals [1,2], forms bubbles at very low concentrations, and degrades the mechanical properties of structural materials over a wide range of temperatures, particularly if the bubbles migrate to high angle grain boundaries [3,4]. Helium generation can lead to void swelling, as gas pressure stabilizes small vacancy clusters [5], making them resistant to thermal annealing [6], with evidence suggesting that gas atoms are always involved in the void nucleation process [7]. It has been shown that fine precipitates dispersed in the material's matrix can disperse helium into smaller bubbles, which can effectively retard the onset of void swelling [5] and limit the amount of helium that can form bubbles on grain boundaries [8]. In oxide dispersion strengthened (ODS) steel and nanostructured ferritic alloys (NFAs) for example, a very large number density of small oxide particles [9] with different chemistries, including $Y_2Ti_2O_7$, Y_2TiO_5, and Y_2O_3 [10–14] are dispersed inside the ferritic matrix and impart creep strength [15–17]. The smallest particles in MA957 and NFA 14YWT are found to be $Y_2Ti_2O_7$ [18], while larger particles in similar materials, or particles found in Eurofer97, are often found to be Y_2O_3 [12]. Recent work featured the development of Fe/$Y_2Ti_2O_7$ interfaces in order to evaluate the interface properties of the smallest particles as they are found in 14YWT [20]. It has been shown that the particle-matrix interface can act as radiation induced point defect sink as well as a sink for helium or nucleation site for helium bubbles [21–25]. Thus, by virtue of the high number density of the oxide particles found in these materials, helium can be effectively dispersed in many small bubbles. Due to the small size of the oxide phase particles [9] and their complex chemistry [26], irradiation stability studies at these interfaces are challenging. Thus, model interfaces with a simplified, but realistic chemistry are often used as templates for irradiation studies [27–31]. In this work, model Fe/Y_2O_3 bilayered systems and associated interfaces with different crystallographic orientations were used as substrates to study the formation of helium bubbles at the metal oxide interface as well as within the oxide and metal phases on either side. In addition, in situ post-implantation heating studies in TEM were performed to investigate bubble growth and possible migration.

Aberration corrected Scanning Transmission Electron Microscopy (STEM) was used to examine helium bubble size and nucleation sites in the metal/oxide bilayer system. Epitaxial thin films of Y_2O_3 were deposited on yttria-stabilized zirconia (YSZ, zirconia containing 8% yttria) single crystal substrates with ⟨100⟩ and ⟨110⟩ orientations that were purchased commercially. Depositions of the Y_2O_3 films were performed by pulsed laser deposition from a pure Y_2O_3 target. After the Y_2O_3 depositions, the samples were loaded into an ultra-high vacuum (UHV) molecular beam epitaxy (MBE) system for Fe film deposition. Potential carbon contamination was removed by exposure to activated oxygen generated in an electron cyclotron resonance microwave plasma source at room temperature. Samples were then heated to ~550 °C for deposition of Fe film (to a nominal thickness of 40 nm) from an effusion cell (flux rate 0.012 nm/s). Reflection high energy electron diffraction (RHEED) patterns were monitored for crystalline order of the cleaned Y_2O_3 surface and the subsequent Fe film deposition. Thin (~65 nm) TEM specimen were

* Corresponding author at: Applied Materials Inc., Sunnyvale, CA 94085, USA.
E-mail address: alexander_mairov@amat.com (A. Mairov).
[1] Present address: Materials Science and Technology Division, Los Alamos National Laboratory, Los Alamos, NM 87545.

https://doi.org/10.1016/j.scriptamat.2018.11.006
1359-6462/

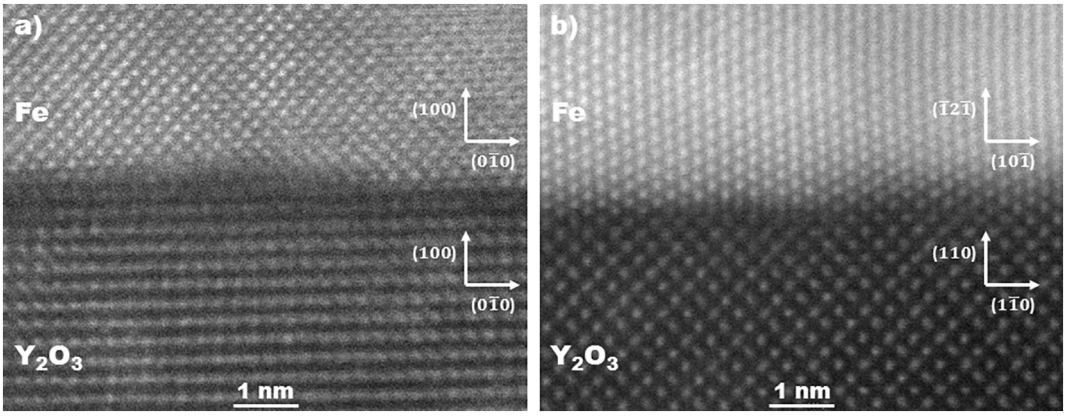

Fig. 1. Aberration corrected STEM images of as deposited Fe/Y_2O_3 interfaces in the following orientation relationships: (a) $[001]_{Y_2O_3}\|[001]_{Fe}$ & $(100)_{Y_2O_3}(100)_{Fe}$ and (b) $[001]_{Y_2O_3}\|[111]_{Fe}$ &$(110)_{Y_2O_3}(\bar{1}2\bar{1})_{Fe}$.

prepared with a Zeiss Auriga Focused Ion Beam FE SEM and implanted with helium ions with a Zeiss ORION nanofab helium microscope at the University of California, Berkeley. Implantations were performed directly into the TEM foil at room temperature to a nominal dose of 10^{18} ions/cm^2 with a current of ~100 pA and ions energy of 25 KeV. SRIM simulations [32] – not shown – were also performed to determine the He concentration in the layered system. Average He concentration in both the layers was found to be comparable, with a peak He concentration of ~17% and 18% for the Fe and Y_2O_3 layers respectively. Parameters for the simulations were displacement energies of 40 eV for Fe, 25 for Y and 28 for O, a sample thickness of 65 nm for both the layers and ion energies of 25 KeV.

Orientation relationships (ORs) between the Fe and the Y_2O_3 layers were determined using Fast Fourier Transform (FFT) of the STEM images. STEM imaging of voids and bubbles was preferred over the conventional Fresnel contrast method as the identification of small bubbles close to interphase boundaries in conventional TEM is complicated by spherical aberration and defocus effects [33]. A heating experiment was carried out inside the TEM (JEOL 3010) using a Gatan 628 single tilt heating stage to 400 °C in-situ with an average heating rate of 4.4 °C/min.

Fig. 1 shows aberration corrected STEM images of as deposited Fe/Y_2O_3 interfaces. Several ORs were found among the samples analyzed, and the $[001]_{Y_2O_3}\|[111]_{Fe}$&$(110)_{Y_2O_3}(\bar{1}2\bar{1})_{Fe}$, found on the samples

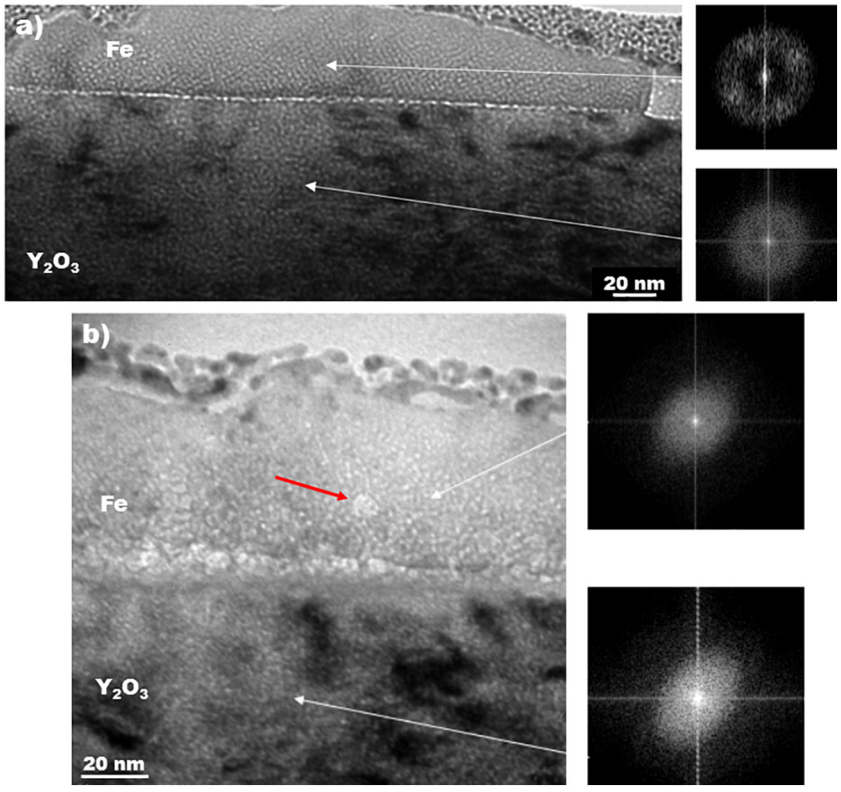

Fig. 2. BF-underfocused images of the as implanted material samples and heated samples. At room temperature (a), both layers show significant amounts of helium bubbles in the material while the Fe layer shows an ordered structure of helium bubbles (as evidenced by the faint spots in the FFT inset). When the same sample is heated to 400 °C (b) the order in the Fe layer is lost (small islands of what likely is Fe-oxide, indicated by a short red arrow, are seen to grow as a result of the heating). The FFT insets are calculated from the respective regions, indicated by the white arrows. (For interpretation of the references to colour in this figure legend, the reader is referred to the web version of this article.)

synthesized on the YSZ(110) substrates, was the most commonly observed one. After helium implantation, helium bubbles were identified within both the thin films and at their interface. Interestingly, it was found that the helium bubbles showed a distinct ordered structure in the Fe layer, while no order in the Y_2O_3 layer was observed. Fig. 2 shows underfocused bright field (BF) TEM images of the Fe $(\bar{1}2\bar{1})_{Fe}$ layer on top of the Y_2O_3 $(110)_{Y_2O_3}$ substrate. The inset shows the FFT calculated from the helium bubble structure in the Fe and in the Y_2O_3. This is not surprising since it is known that helium bubbles tend to arrange themselves in relationship to the host lattice in most materials below $0.2T_m$ and in bcc materials along the [110] host lattice planes [34]. No ordering was observed in the Y_2O_3 film and unfortunately no previous work is available to bench-mark this finding. In the in-situ heating experiment carried out inside the TEM up to 400 °C, it was found that the superlattice is lost in the Fe film while initial growth of what likely is Fe-oxide can be observed. During the heating it was observed that the lattice order still exists at 250 °C while it is lost above that temperature (350 °C and higher). It is known that helium bubble superlattices are lost if the temperature exceeds $0.2T_m$ (361 °C for Fe) and thus the observations in this study are consistent with literature [34].

Fig. 3 shows STEM images where helium bubbles can be identified as black spots due to their lower average Z-number as compared to the surrounding background. As can be seen helium nucleates as small bubbles in both the Y_2O_3 and the Fe layers, and at the interface. The size of helium bubbles is noticeably larger at the interface than in the individual layers, indicating that surface energy minimization effects may favor coalescence of bubbles at the metal/oxide interface.

Statistical analysis yielded the following diameters of the average helium bubble size: $D_{Y2O3} = 1.45 \pm 0.23$ nm, $D_{Fe} = 1.51 \pm 0.25$ nm and $D_{Y2O3/Fe} = 2.23 \pm 0.36$. Thus, the average bubble size is similar in the metal and in the oxide films, but significantly larger at the metal-oxide interface.

Fig. 4 shows several bubbles nucleating on these metal-oxide interfaces and on general grain boundaries in the Fe film. For the Fe film, the bubbles nucleating at grain boundaries are not significantly larger than bubbles nucleating in the grain interior. An increase in bubble size is observed only at the metal/oxide interface. Moreover, bubbles nucleating on the grain boundaries of the Fe film symmetrically form and overlap across the boundary. This is an interesting observation and in contrast to what was observed at the metal/oxide interface, where the bubbles nucleated on the oxide side and only wet this side of the interface. No overlap of the bubbles across the interface was observed for any of the analyzed bubbles at the metal/oxide interface. A similar behavior has been observed in literature for Cu/Ag [35] and Cu/Nb [36,37] interfaces, and explained on the basis of differences in surface energies of the different constituents. Semi-empirical estimates

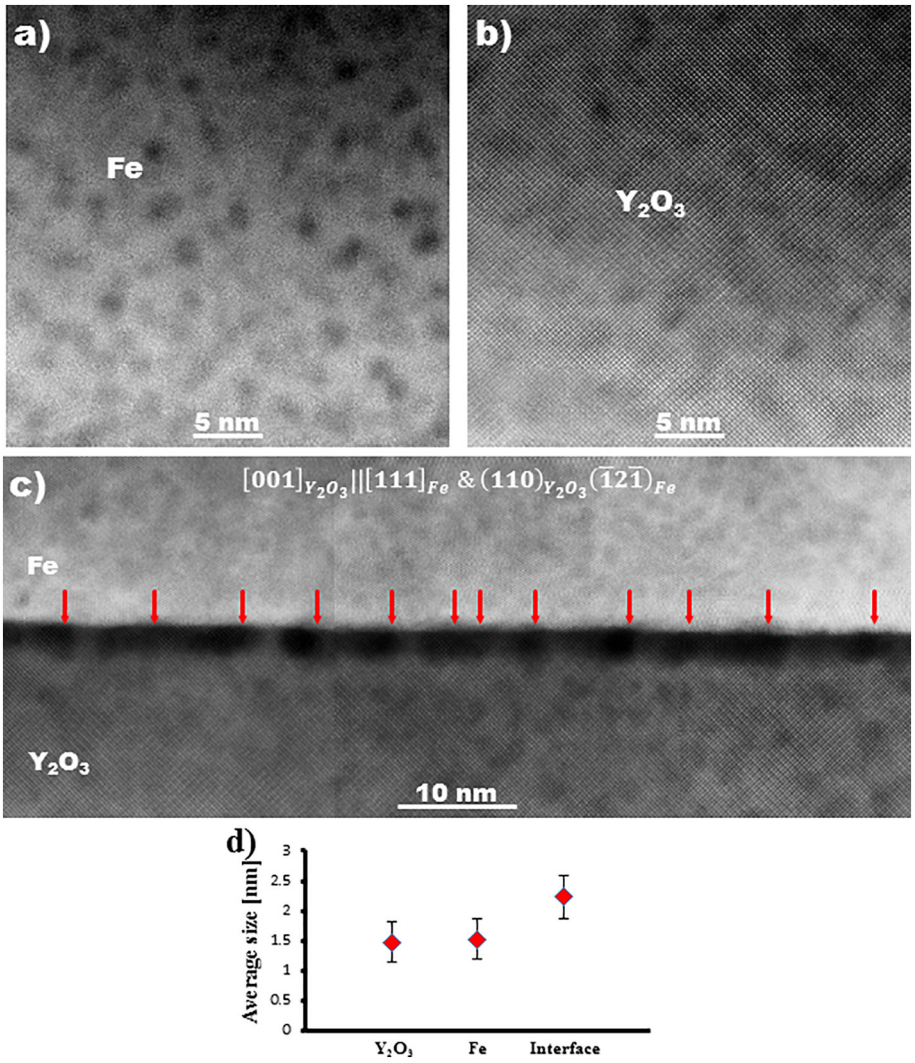

Fig. 3. Aberration corrected STEM images of helium bubbles in (a) iron layer (b) Y_2O_3 layer (c) large section of the metal oxide interface in the $[001]_{Y_2O_3}||[111]_{Fe}$&$(110)_{Y_2O_3}(\bar{1}2\bar{1})_{Fe}$ orientation relationship. (d) The average bubble size is greater at the metal/oxide interface as compared to within the individual layers. Red arrows in (c) indicate some of the bubbles seen at the interface. (For interpretation of the references to colour in this figure legend, the reader is referred to the web version of this article.)

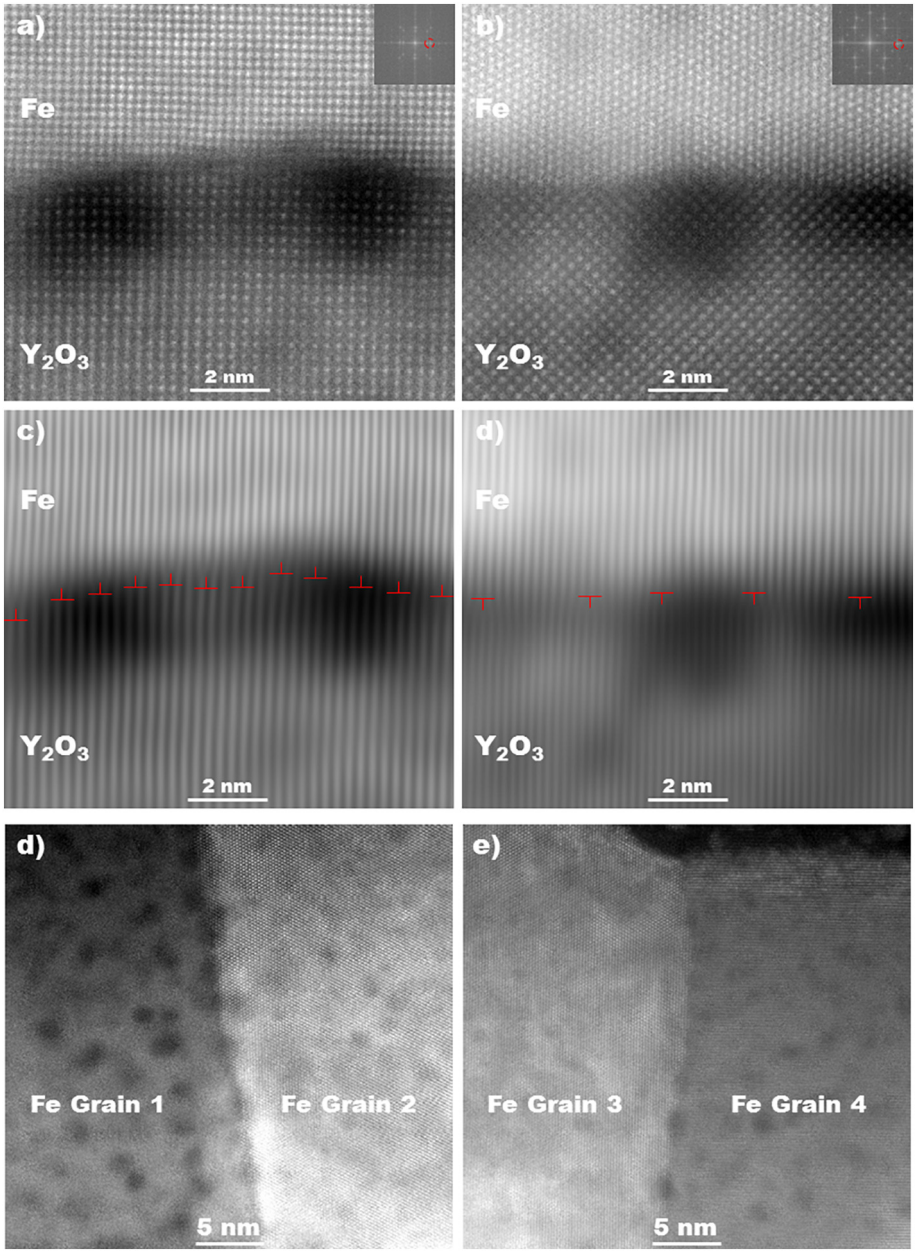

Fig. 4. Aberration corrected STEM images of helium bubbles in (a) YSZ(100)/Y_2O_3/Fe interface with $[001]_{Y_2O_3}\|[001]_{Fe}$&$(100)_{Y_2O_3}(\bar{1}\bar{1}0)_{Fe}$ OR and (b) YSZ(110)/Y_2O_3/Fe with $[001]_{Y_2O_3}\|[111]_{Fe}$&$(110)_{Y_2O_3}(\bar{1}2\bar{1})_{Fe}$ OR. (c and d) are the iFFT images obtained with the spots shown in the insets of (a) and (b). The bubbles preferentially nucleate on the oxide film side and only wet the interface, even when misfit dislocations are located on the Fe side of the interface, as shown in (c). (e and f) show bubbles nucleating at two different grain boundaries in the Fe layer.

of the surface energy of iron varies between 2.42 J/m^2 [38] and 2.48 J/m^2 [39], while DFT simulations yield values ranging between 2.22 J/m^2 and 2.73 J/m^2 [40], depending on the specific surface. Since the interface is the Fe surface, it is appropriate to use the surface energy instead of GB energy which has a maximum value of 1.2 J/m^2 for a non-specific GB [41]. The surface energy of Y_2O_3 crystals is quoted as 1.66 J/m^2 [42] which is significantly lower than the values for Fe surfaces. Because of its lower surface energy, bubbles are expected to nucleate on the oxide side and only wet the metal/oxide interface. Nucleation of bubbles contained in both the individual layers is then most likely due to the very high dose injected inside the sample and the existence of only one interface. If a multilayered film structure is to be synthesized, with a relatively small individual layer thickness, or a higher temperature irradiation is to be performed, it is likely that bubbles would nucleate only at the metal/oxide interfaces (towards the Y_2O_3 side). An estimation of the lowest bound for the metal/oxide interfacial energy can be determined using the wetting parameter W:

$$W = \gamma_A + \gamma_{AB} - \gamma_B \quad (1)$$

with $\gamma_A < \gamma_B$, where γ_A and γ_B are the surface energies of the two constituents and $\gamma_{AB}$is the interfacial energy. Since wetting is favored when W > 0, by using Eq. (1), a lowest bound for the energy value of 0.56 J/m^2 can be set for these interfaces. This value falls within the interval of energies expected for semi-coherent interfaces [43].

The relatively high lattice mismatch between the two films also causes the formation of a very high density of misfit dislocations (MDs) at the interface. Nonetheless, the interfacial bubbles always nucleate on the oxide side of the interface, even when several MDs are observed to be located on the Fe side of the interface, as shown in Fig. 4.

Moreover, it appears from the high-resolution images that, occasionally, the interface initially flat becomes wavy as a result of the presence of the bubbles. Even in this case, bubbles do not overlap across the interface, as can be seen by the bubble surface which clearly terminates within the Y_2O_3 film. It must be noted that recent work performed on Cu/Nb bulk nanolayered composites fabricated by accumulative roll bonding (ARB), have shown that layer thickness and temperature can dictate whether the cavities cross the interface following He implantation [44]. It would be interesting to extend studies on metal/oxide interfaces to similar regimes, to evaluate if similar behaviors can be observed.

Statistical analysis of the bubble size did not yield a significant difference for different ORs and between interfaces with specific ORs and incoherent interfaces. Moreover, bubbles were seen to nucleate at random locations at the interface, and not at specific sites such as MDs, which theory predicts to be preferential nucleation sites. However, it must be noted that for the synthesized interfaces, MDs density was extremely high, so it would not be probable for bubbles to nucleate at every MD. Although a difference in bubble size is expected to be a function of the interface character, the fact that the metal/oxide interface in general is effective in sequestrating helium is a valuable observation. ODS steels and NFAs being considered for nuclear reactors will in fact have nanometer-size scaled oxide particles with a broad range of interfacial characteristics. The observation that all metal/oxide interfaces can be potentially effective nucleation sites for helium bubbles, independently of their interfacial character, supports the ability of these alloys to effectively disperse large concentrations of helium in many small bubbles and to effectively resist helium embrittlement and swelling. Moreover, bubbles observed at grain boundaries in the Fe layer were observed to have a size comparable to bubbles observed in the interior of the Fe grains. These observations confirm the metal/oxide interface to be very efficient site for helium bubble nucleation and even more so than grain boundaries in the metal matrix. Finally, bubbles nucleating at the metal/oxide interface nucleate from the oxide side and only wet the interface, never growing across this boundary. This is due to the differences in the surface energies of the oxide and the metal films, and confirms the intrinsically different character of these interfaces, as compared to grain boundaries.

These observations have important implications on how the helium bubbles will be distributed in the nanostructure of ODS steels and NFAs and the role of the oxide nanoparticle size in the overall capacity of these materials to absorb helium bubbles warrants further experimental investigation. Thus, the presence of a large number of oxide particles inside the matrix is indeed very beneficial in sequestering helium and retarding or even suppressing embrittlement caused by helium bubble formation and accumulation at various sites.

In conclusion, the direct helium implantation on specifically designed Fe/Y_2O_3 interfaces leads to results which can aid in a better understanding of helium management in ODS and NFA materials systems. It was found that a helium superlattice is present in the Fe layer but not in the Y_2O_3 layer after room temperature helium implantation. The superlattice structure is lost at annealing temperatures above 250 °C, which is in agreement with the literature. Large helium bubbles nucleate at the Y_2O_3/Fe interface regardless of the OR between the Fe and the Y_2O_3 layers and of the interface character. The helium bubbles nucleating at the interface are all within the Y_2O_3 film, which can be attributed to its reduced surface energy as compared to the Fe layer. Furthermore, the observed behavior is in agreement with the hypothesis that oxide particles in a ferritic steel matrix can accommodate large amount of helium.

Acknowledgements

The samples were helium-implanted at the Biomolecular Nanotechnology Center/QB3 at UC Berkeley utilizing the NSF-MRI funded ORION Nanofab.

The TEM in-situ heating was performed at The Molecular Foundry, which is supported by the Office of Science, Office of Basic Energy Sciences, of the U.S. Department of Energy under Contract No. DEAC02-05CH11231. Funding for Helium implantation was provided from NSF/DMRMRI1338139.

References

[1] J. Laakmann, P. Jung, W. Uelhoff, Acta Metall. 35 (1987) 2063–2069.
[2] K. Morishita, R. Sugano, B.D. Wirth, J. Nucl. Mater. 323 (2003) 243–250.
[3] S.J. Zinkle, G.S. Was, Acta Mater. 61 (2013) 735–758.
[4] H. Trinkaus, B.N. Singh, J. Nucl. Mater. 323 (2003) 229–242.
[5] G.R. Odette, M.J. Alinger, B.D. Wirth, Annu. Rev. Mater. Res. 38 (2008) 471–503.
[6] G.R. Odette, P.J. Maziasz, J.A. Spitznagel, J. Nucl. Mater. 104 (1981) 1289–1303.
[7] G.S. Was, Fundamentals of Radiation Materials Science: Metals and Alloys, (New York) 2007.
[8] L. Yang, Y. Jiang, Y. Wu, G.R. Odette, Z. Zhou, Z. Lu, Acta Mater. 103 (2016) 474–482.
[9] M.C. Brandes, L. Kovarik, M.K. Miller, M.J. Mills, J. Mater. Sci. 47 (2012) 3913–3923.
[10] S. Ukai, T. Okuda, M. Fujiwara, T. Kobayashi, S. Mizuta, H. Nakashima, J. Nucl. Sci. Technol. 39 (2002) 872–879.
[11] S. Yamashita, S. Ohtsuka, N. Akasaka, S. Ukai, S. Ohnuki, Philos. Mag. Lett. 84 (2004) 525–529.
[12] M. Klimiankou, R. Lindau, A. Möslang, J. Cryst. Growth 249 (2003) 381–387.
[13] M. Klimiankou, R. Lindau, A. Moslang, J. Nucl. Mater. 329–333 (2004) 347–351.
[14] M. Klimiankou, R. Lindau, A. Möslang, Micron 36 (2005) 1–8.
[15] T. Hayashi, P.M. Sarosi, J.H. Schneibel, M.J. Mills, Acta Mater. 56 (2008) 1407–1416.
[16] M.C. Brandes, L. Kovarik, M.K. Miller, G.S. Daehn, M.J. Mills, Acta Mater. 60 (2012) 1827–1839.
[17] S. Ukai, M. Fujiwara, R.L. Klueh, P.J. Maziasz, I.S. Kim, L. Heatherly, D.T. Hoelzer, N. Hashimoto, E.A. Kenik, K. Miyahara, J. Nucl. Mater. 307–311 (2002) 749–757.
[18] Y. Wu, J. Ciston, S. Kraemer, N. Bailey, G.R. Odette, P. Hosemann, Acta Mater. 111 (2016) 108–115.
[20] G.R.O.T. Stan, Y. Wu, P.B. Wells, H.D. Zhou, Metall. Mater. Trans. A 48 (2017) 5658–5666.
[21] P.D. Edmondson, C.M. Parish, Y. Zhang, A. Hallén, M.K. Miller, Scr. Mater. 65 (2011) 731–734.
[22] P.D. Edmondson, C.M. Parish, Y. Zhang, A. Hallén, M.K. Miller, J. Nucl. Mater. 434 (2013) 210–216.
[23] T. Chen, J.G. Gigax, L. Price, D. Chen, S. Ukai, E. Aydogan, S.A. Maloy, F.A. Garner, L. Shao, Acta Mater. 116 (2016) 29–42.
[24] J. Chen, P. Jung, W. Hoffelner, H. Ullmaier, Acta Mater. 56 (2008) 250–258.
[25] C.H. Zhang, Y.T. Yang, Y. Song, J. Chen, L.Q. Zhang, J. Jang, A. Kimura, J. Nucl. Mater. 455 (2014) 61–67.
[26] S. Choudhury, J.A. Aguiar, M.J. Fluss, L.L. Hsiung, A. Misra, B.P. Uberuaga, Sci. Rep. 5 (2015) 13086.
[27] T. Stan, Y. Wu, G.R. Odette, K.E. Sickafus, H.A. Dabkowska, B.D. Gaulin, Metall. Mater. Trans. A Phys. Metall. Mater. Sci. 44 (2013) 4505–4512.
[28] E.B. Watkins, A. Kashinath, P. Wang, J.K. Baldwin, J. Majewski, M.J. Demkowicz, Appl. Phys. Lett. 105 (2014), 041601. .
[29] T.C. Kaspar, M.E. Bowden, C.M. Wang, V. Shutthanandan, N.R. Overman, R.M. van Ginhoven, B.D. Wirth, R.J. Kurtz, J. Nucl. Mater. 457 (2015) 352–361.
[30] Y. Xu, J.A. Aguiar, S.K. Yadav, O. Anderoglu, J.K. Baldwin, Y.Q. Wang, J.A. Valdez, A. Misra, H.M. Luo, B.P. Uberuaga, N. Li, Acta Mater. 89 (2015) 364–373.
[31] J.A. Aguiar, O. Anderoglu, S. Choudhury, J.K. Baldwin, Y. Wang, A. Misra, B.P. Uberuaga, J. Mater. Sci. 50 (2015) 2726–2734.
[32] J.F. Ziegler, J. Biersack, U. Littmark, The Stopping and Range of Ions in Matter, Pergamon Press, New York, 1985.
[33] T. Stan, Y. Wu, T. Brown, C. Palmstrom, G.R. Odette, F. Allen, P. Hosemann, Fusion React. Mater. Progr. 59 (2015) 64–70.
[34] P.B. Johnson, D.J. Mazey, J. Nucl. Mater. 218 (1995) 273–288.
[35] S. Zheng, S. Shao, J. Zhang, Y. Wang, M.J. Demkowicz, I.J. Beyerlein, N.A. Mara, Sci. Rep. 5 (2015) 15428.
[36] K. Hattar, M.J. Demkowicz, A. Misra, I.M. Robertson, R.G. Hoagland, Scr. Mater. 58 (2008) 541–544.
[37] W.Z. Han, N.A. Mara, Y.Q. Wang, A. Misra, M.J. Demkowicz, J. Nucl. Mater. 452 (2014) 57–60.
[38] W.R. Tyson, W.A. Miller, Surf. Sci. 62 (1977) 267–276.
[39] F.R. de Boer, R. Boom, W.C.M. Mattens, A.R. Miedema, A.K. Niessen, Cohesion in Metals: Transition Metals and Alloys, Elsevier, Amsterdam, 1988.
[40] L. Vitos, A.V. Ruban, H.L. Skriver, J. Kollár, Surf. Sci. 411 (1998) 186–202.
[41] S. Ratanaphan, D.L. Olmsted, V.V. Bulatov, E.A. Holm, A.D. Rollett, G.S. Rohrer, Acta Mater. 88 (2015) 346–354.
[42] P. Zhang, A. Navrotsky, B. Guo, I. Kennedy, A.N. Clark, C. Lesher, Q. Liu, J. Phys. Chem. C 112 (2008) 932–938.
[43] J.H. Howe, Interfaces in Materials: Atomic Structure, Thermodynamics and Kinetics of Solid-Vapor, Solid-Liquid and Solid-Solid Interfaces, Wiley, 1997.
[44] L.X. Yang, S.J. Zheng, Y.T. Zhou, J. Zhang, Y.Q. Wang, C.B. Jiang, N.A. Mara, I.J. Beyerlein, X.L. Ma, J. Nucl. Mater. 487 (2017) 311–316.